The ALMA Survey of 70 μm Dark High-mass Clumps in Early Stages (ASHES). VI. The Core-scale CO Depletion

(article starts on next page)

The ALMA Survey of 70 μm Dark High-mass Clumps in Early Stages (ASHES). VI. The Core-scale CO Depletion

Giovanni Sabatini[1] , Stefano Bovino[1,2] , Patricio Sanhueza[3,4] , Kaho Morii[3,5] , Shanghuo Li[6] , Elena Redaelli[7] ,
Qizhou Zhang[8] , Xing Lu[9] , Siyi Feng[10] , Daniel Tafoya[11] , Natsuko Izumi[12] , Takeshi Sakai[13] ,
Ken'ichi Tatematsu[4,14] , and David Allingham[15]

[1] INAF—Istituto di Radioastronomia—Italian node of the ALMA Regional Centre (It-ARC), Via Gobetti 101, I-40129 Bologna, Italy
[2] Departamento de Astronomía, Facultad Ciencias Físicas y Matemáticas, Universidad de Concepción, Av. Esteban Iturra s/n Barrio Universitario, Casilla 160,
Concepción, Chile
[3] National Astronomical Observatory of Japan, National Institutes of Natural Sciences, 2-21-1 Osawa, Mitaka, Tokyo 181-8588, Japan
[4] Department of Astronomical Science, The Graduate University for Advanced Studies, SOKENDAI, 2-21-1 Osawa, Mitaka, Tokyo 181-8588, Japan
[5] Department of Astronomy, Graduate School of Science, The University of Tokyo, 7-3-1 Hongo, Bunkyo-ku, Tokyo 113-0033, Japan
[6] Korea Astronomy and Space Science Institute, 776 Daedeokdae-ro, Yuseong-gu, Daejeon 34055, Republic Of Korea
[7] Max-Planck-Institut für extraterrestrische Physik, Gießenbachstraße 1, D-85749 Garching bei München, Germany
[8] Center for Astrophysics, Harvard & Smithsonian, 60 Garden Street, Cambridge, MA 02138, USA
[9] Shanghai Astronomical Observatory, Chinese Academy of Sciences, 80 Nandan Road, Shanghai 200030, People's Republic of China
[10] Department of Astronomy, Xiamen University, Zengcuo'an West Road, Xiamen, 361005 People's Republic of China
[11] Department of Space, Earth and Environment, Chalmers University of Technology, Onsala Space Observatory, SE-43992 Onsala, Sweden
[12] Academia Sinica Institute of Astronomy and Astrophysics, No. 1, Section 4, Roosevelt Road, Taipei 10617, Taiwan, Republic of China
[13] Graduate School of Informatics and Engineering, The University of Electro-Communications, Chofu, Tokyo 182-8585, Japan
[14] Nobeyama Radio Observatory, National Astronomical Observatory of Japan, National Institutes of Natural Sciences, 462-2 Nobeyama, Minamimaki, Minamisaku,
Nagano 384-1305, Japan
[15] School of Mathematical and Physical Sciences, University of Newcastle, University Drive, Callaghan, NSW 2308, Australia

Abstract

Studying the physical and chemical properties of cold and dense molecular clouds is crucial for the understanding of how stars form. Under the typical conditions of infrared dark clouds, CO is removed from the gas phase and trapped onto the surface of dust grains by the so-called depletion process. This suggests that the CO-depletion factor (f_D) can be a useful chemical indicator for identifying cold and dense regions (i.e., prestellar cores). We have used the 1.3 mm continuum and $C^{18}O$ (2–1) data observed at the resolution of ∼5000 au in the ALMA Survey of 70 μm Dark High-mass Clumps in Early Stages (ASHES) to construct averaged maps of f_D in 12 clumps to characterize the earliest stages of the high-mass star formation process. The average f_D determined for 277 of the 294 ASHES cores follows an unexpected increase from the prestellar to the protostellar stage. If we exclude the temperature effect due to the slight variations in the NH_3 kinetic temperature among different cores, we explain this result as a dependence primarily on the average gas density, which increases in cores where protostellar conditions prevail. This shows that f_D determined in high-mass star-forming regions at the core scale is insufficient to distinguish among prestellar and protostellar conditions for the individual cores and should be complemented by information provided by additional tracers. However, we confirm that the clump-averaged f_D values correlate with the luminosity-to-mass ratio of each source, which is known to trace the evolution of the star formation process.

Supporting material: machine-readable table

1. Introduction

Although high-mass stars ($M > 8$–$10\,M_{\odot}$) represent a small fraction compared to less massive counterparts, they play a major role in shaping the physical and chemical properties of the interstellar medium (ISM). The formation of H II regions at the end of the high-mass star formation process may favor conditions for triggering a secondary star formation cycle (Elmegreen 1998), involving molecular gas that is richer in complex organic molecules (COMs; Herbst & van Dishoeck 2009), a large number discovered in the hot molecular cores around massive young stellar objects (mYSOs; e.g., Kurtz et al. 2000; Cesaroni 2005). There is also evidence that the Sun was formed in a cluster that originally hosted high-mass stars (e.g., Adams 2010). Therefore, studying the details of the formation process of high-mass stars is crucial to understand how the chemical composition of the ISM evolves and how life arises from the organic materials produced during the star formation process.

In the past few decades, several theoretical scenarios have been proposed to describe the high-mass star formation process (e.g., Bonnell et al. 2001; McKee & Tan 2002; Tigé et al. 2017; Kumar et al. 2020; Padoan et al. 2020). These scenarios differ in the initial physical assumptions and predict different formation timescales. The identification and systematic study of the early stages of the high-mass star formation process, before the formation of mYSO (s), is hence crucial for distinguishing between the many existing scenarios (e.g., Zhang et al. 2009; Zhang & Wang 2011; Wang et al. 2014; Sanhueza et al. 2017, 2019).

Infrared dark clouds (IRDCs), originally identified in absorption against the galactic background in the mid-IR at

8 μm (e.g., Perault et al. 1996; Egan et al. 1998), are so far considered the most likely birthplaces of high-mass stars. These are ubiquitous and extended (>10 pc) filamentary structures throughout the Galactic disk, which fragment into clumps and cores, with typical sizes of ~1 pc and ≲0.1 pc, respectively (e.g., Carey et al. 1998; Rathborne et al. 2006; Simon et al. 2006a, 2006b; Battersby et al. 2010; Peretto et al. 2016; Pokhrel et al. 2018; Li et al. 2022; Chevance et al. 2022). By combining the IR and radio continuum properties obtained from several galactic plane surveys (e.g., MSX, Price et al. 2001; MIPSGAL, Carey et al. 2009; rms, Urquhart et al. 2009; ATLASGAL, Schuller et al. 2009; Hi-GAL, Molinari et al. 2010; CORNISH, Hoare et al. 2012),[16] clumps can be classified into evolutionary stages.

As originally reported by Saraceno et al. (1996) for the low-mass regime, the high-mass clumps belonging to different phases also lie in different regions of the L–M diagram (see Molinari et al. 2008), which compares the circumstellar envelope mass (M) and the bolometric luminosity (L) for a given clump. The luminosity-to-mass ratio (L/M) of the clumps increases from the prestellar to the more evolved H II stage as a signature of forming mYSOs and has therefore been used as an additional diagnostic tool to identify clumps at different evolutionary stages (e.g., Molinari et al. 2008; Elia et al. 2017; Giannetti et al. 2017b; Urquhart et al. 2018, 2022; Sabatini et al. 2021). According to this general scheme, clumps that lack 24 and 70 μm emission also show a lower L/M ratio and are usually associated with the quiescent/prestellar stage (e.g., Zhang et al. 2014; Chambers et al. 2009; Sanhueza et al. 2012, 2013, 2019; Guzmán et al. 2015). However, even under these conditions, it is not possible to completely rule out the presence of star-forming activity in these clumps, which can reveal the presence of cores at different evolutionary stages when observed at high resolution (e.g., Feng et al. 2016b; Li et al. 2019, 2020; Sanhueza et al. 2019; Morii et al. 2021; Tafoya et al. 2021; Sakai et al. 2022).

Additional chemical constraints have been proposed over time to better characterize the evolutionary picture of the high-mass star formation process. Under the typical physical conditions of dense regions in IRDCs, $n(H_2) \gtrsim 10^4$ cm^{-3} and $T_{gas} \lesssim 20$ K, a well-known example of chemical constraint is given by the estimates of the CO depletion (e.g., Kramer et al. 1999; Bergin et al. 2002; Caselli et al. 2008; Wiles et al. 2016; Sabatini et al. 2019; Feng et al. 2020), which has been used in particular to identify the youngest clumps (e.g., Fontani et al. 2006; Pillai et al. 2007; Giannetti et al. 2014).

How much of CO is depleting onto the surface of dust grains is usually characterized by the depletion factor (e.g., Caselli et al. 1999; Fontani et al. 2012; Sabatini et al. 2019), defined as the ratio between the expected CO/H$_2$ abundance (X_{CO}^E) and the observed one (X_{CO}^O):

$$f_D = \frac{X_{CO}^E}{X_{CO}^O} = \frac{X_{CO}^E \, N(H_2)}{N(CO)}, \qquad (1)$$

where $N(H_2)$ and $N(CO)$ are the H$_2$ and CO column density, respectively. CO-depletion factors of up to a few tens have

been derived on clump scales in various samples of young, high-mass star-forming regions (e.g., Thomas & Fuller 2008; Fontani et al. 2012; Feng et al. 2016a, 2020). The estimation of f_D could be a suitable and convenient way to identify the cold/prestellar gas also at core scales. However, very few and isolated estimates of f_D on these scales are found in the literature in high-mass star-forming regions, with extreme values of f_D up to 100–1000 (Zhang et al. 2009; Morii et al. 2021; Rodríguez et al. 2021). In the absence of additional evidence for the high-mass regime, in this study we aim to test whether the CO-depletion factor can be considered a reliable tracer for cores at different evolutionary stages, embedded in high-mass star-forming regions.

This work is structured as follows: In Section 2 we describe the sample and the data set on which this study is based. In Section 3 we report on the derivation of the maps of $N(H_2)$ and C^{18}O used to construct the final f_D maps. In Section 4 we discuss the variation in the averaged f_D obtained for a population of cores at different evolutionary stages. Finally, in Section 5 we summarize our conclusions.

2. Sample and Data Reduction

The ALMA[17] Survey of 70 μm Dark High-mass Clumps in Early Stages (ASHES; Sanhueza et al. 2019) provides an ideal basis for detailed studies of the earliest stages of the high-mass star formation process. In a pilot study (Sanhueza et al. 2019), 12 massive 70 μm dark clumps were mosaicked with ALMA in the dust continuum at ~224 GHz (~1″.2 resolution) and used to characterize clump fragmentation (Table 1). We refer to Sanhueza et al. (2019) for a detailed description of the source selection criteria. From the dust continuum, a total of 294 cores were detected (excluding those located at the edges of the observed fields—i.e., ~20%–30% power point—where flux estimates are more uncertain).[18] ASHES was designed to map the molecular emission of a large number of molecules in the ALMA Band-6, including CO, C^{18}O, H$_2$CO, CH$_3$OH, SiO, ^{13}CS, N$_2$D$^+$, DCN, DCO$^+$, and CCD. These tracers are used to characterize cores from a chemical point of view, allowing their classification into different evolutionary stages (see Li et al. 2020; Morii et al. 2021; Tafoya et al. 2021; Sakai et al. 2022; S. Li et al. 2022, in preparation).

Of the total population of 294 cores, ~71% of cores (210 cores) are classified as prestellar, lacking any star formation signatures, while ~29% (84 cores) are classified as protostellar candidates, being associated with molecular outflows and/or "warm core" line emission (i.e., H$_2$CO and CH$_3$OH lines with high upper energy levels).

Since different chemical conditions were assumed for the identification of the protostellar cores, they were additionally divided into three categories (Sanhueza et al. 2019; Li et al. 2020): (1) Cores with molecular outflows (i.e., 24 cores, corresponding to ~8% of the total population) identified via CO, SiO, and/or H$_2$CO lines and in which no "warm cores" lines were detected. (2) "Warm cores" (34 cores, ~12%) representing an evolutionary phase prior to the hot molecular core phase typically found to be associated with high-mass protostars. This class lacks in molecular

---

Table 1
Summary of the Physical and Chemical Properties of the ASHES Sources

Clump-ID	$d_\odot$[a]	R_{GC}[a]	Mass[b]	R_{eff}[c]	rms (mJy beam^{-1})[d]		$(V_{lsr}^{C^{18}O})$[e]	$(\sigma^{C^{18}O})$[e]	γ[f]	$(X_{C^{18}O}^E)$[g]	f_D[h]
	(kpc)	(kpc)	($M_\odot$)	(arcsec)	1.3 mm	$C^{18}O$ (2–1)	(km s^{-1})	(km s^{-1})			
(1)	(2)	(3)	(4)	(5)	(6)	(7)	(8)	(9)	(10)	(11)	(12)
G010.991–00.082	3.7	4.91	2230	27	0.115	5.150	29.5 ± 0.3	0.7 ± 0.3	74	5.5×10^{-7}	2.8
G014.492–00.139	3.9	4.79	5200	23	0.168	5.200	41.2 ± 0.2	0.8 ± 0.2	72	5.7×10^{-7}	4.6
G028.273–00.167	5.1	4.73	1520	24	0.164	5.310	80.2 ± 0.2	0.8 ± 0.2	71	5.9×10^{-7}	3.5
G327.116–00.294	3.9	5.63	580	20	0.089	4.150	-58.8 ± 0.2	0.7 ± 0.2	85	4.3×10^{-7}	1.9
G331.372–00.116	5.4	4.56	1640	24	0.083	4.270	-87.8 ± 0.1	0.6 ± 0.1	69	6.3×10^{-7}	1.6
G332.969–00.029	4.4	5.03	730	28	0.080	4.320	-66.5 ± 0.2	0.7 ± 0.2	75	5.3×10^{-7}	1.2
G337.541–00.082	4.0	5.08	1180	22	0.068	3.220	-54.6 ± 0.1	0.6 ± 0.1	76	5.2×10^{-7}	2.1
G340.179–00.242	4.1	4.87	1470	37	0.094	5.190	-51.8 ± 0.2	0.8 ± 0.2	73	5.6×10^{-7}	1.1
G340.222–00.167	4.0	4.96	760	19	0.112	5.490	-51.7 ± 0.1	0.7 ± 0.1	74	5.4×10^{-7}	1.2
G340.232–00.146	3.9	4.98	710	25	0.139	5.440	-50.5 ± 0.1	0.8 ± 0.1	75	5.3×10^{-7}	1.7
G341.039–00.114	3.6	5.23	1070	27	0.070	3.340	-43.4 ± 0.1	0.7 ± 0.1	79	4.9×10^{-7}	1.1
G343.489–00.416	2.9	5.75	810	29	0.068	3.480	-28.6 ± 0.1	0.5 ± 0.1	87	4.1×10^{-7}	1.9

Notes.
[a] Taken from Whitaker et al. (2017).
[b] Derived from the Millimetre Astronomy Legacy Team 90 GHz (MALT90) Survey (Contreras et al. 2017).
[c] The clump's effective radius was derived in Sanhueza et al. (2019) from Gaussian fitting to the ATLASGAL dust continuum emission at 870 μm.
[d] The rms of dust continuum emission at 1.3 mm are taken from Sanhueza et al. (2019), while those of $C^{18}O$ are computed from the data cubes presented in Section 2.
[e] Median local standard of rest velocities ($V_{lsr}^{C^{18}O}$) and the velocity dispersions ($\sigma^{C^{18}O}$) obtained from the $C^{18}O$ (2–1) employing the Python Spectroscopic Toolkit (PySpecKit; Ginsburg & Mirocha 2011; Ginsburg et al. 2022; see also Appendix A).
[f] Gas-to-dust ratio derived using Equation (3) (see Section 3.1).
[g] Expected $C^{18}O/H_2$ abundance derived using Equation (6) (see Section 3.3).
[h] Average f_D of each clump determined following the procedure discussed in Section 4.

outflow emission but shows a detection in one of the "warm cores" lines among H_2CO $J = 3_{2,2} - 2_{2,1}(E_u/k_B = 68.09$ K, where k_B is Boltzmann's constant) and $J = 3_{2,1} - 2_{2,0}(E_u/k_B = 68.11$ K), and the CH_3OH $J_k = 4_{2,2} - 3_{1,2}$ ($E_u/k_B = 45.46$ K); (3) The remaining 26 cores (i.e., 9%) presumably belong to a more evolved protostellar stage with both molecular outflow and "warm cores" line detection.

So far, the ASHES project gives access to the largest population of prestellar cores candidates, that have been detected in high-mass star-forming clumps via a mix of dust continuum and line emission data and reveals that even high-mass 70 μm dark clumps can harbor a tiny fraction of deeply embedded cores with nascent star formation activity.

2.1. Observations

ALMA Band-6 observations were carried out in Cycles 3 and 4 (Project 2015.1.01539.S PI: P. Sanhueza) with the 12 m Array (Main Array, MA; Wootten & Thompson 2009) and the 7 m Array (Atacama Compact Array, ACA; Iguchi et al. 2009). Depending on the observed source, the 12 m array included 36–48 antennas distributed over baselines ranging between 15 and 700 m. The Atacama Compact Array includes 7–10 antennas, with baselines between 8 and 48 m. The average angular scales covered by these configurations range from a resolution of $\sim1''25$ to a maximum recoverable scale of $\sim19''$. These scales correspond to spatial scales of $\sim(5-70) \times 10^3$ au at the average distance of 4 kpc.

At the frequency of the $C^{18}O$ (2–1) line, $\nu_{2,1} \sim 219.5$ GHz, the typical 1σ is 5 mJy beam^{-1} (see Table 1), for a channel width of ~0.67 km s^{-1}. The data were calibrated with the Common Astronomy Software Applications (CASA) versions 4.5.3, 4.6, and 4.7, while the CASA version 5.4 was employed for imaging. The $C^{18}O$ cubes were produced using the automatic masking procedure yclean (Contreras et al. 2018). We refer to Sanhueza et al. (2019) for a more detailed description of the data set.

3. Analysis and Results

Based on Equation (1), the derivation of f_D requires the evaluation of the H_2 and CO column densities. Since the main CO isotopologue (i.e., $^{12}C^{16}O$) is almost always optically thick (e.g., Heyer & Dame 2015), its intensity is not proportional to N(CO). Therefore, a less abundant CO isotopologue (i.e., $C^{18}O$) should be used to obtain a much more accurate estimate of f_D. In this section, we summarize the procedure and the assumptions we follow to derive f_D.

3.1. H_2 Column Density Maps

The beam-averaged H_2 column density is computed in each pixel from the primary beam (PB) corrected ALMA continuum flux density at 1.3 mm, $F_{1.3\,mm}$, as (e.g., Schuller et al. 2009)

$$N(H_2) = \frac{F_{1.3\,mm}\gamma}{B_{1.3\,mm}(T_{dust})\,\Omega_{app}\,\kappa_{1.3\,mm}\,\mu_{H_2}\,m_H}, \quad (2)$$

where $B_{1.3\,mm}(T_{dust})$ is the Planck function at 1.3 mm with a dust temperature T_{dust}, Ω_{app} is the beam solid angle,[19] $\mu_{H_2} = 2.8$ is the H_2 mean molecular weight (Kauffmann et al. 2008; see their Section A.1), and m_H is the mass of the hydrogen atom. We adopt a value of $\kappa_{1.3\,mm} = 0.9$ cm^2 g^{-1}, which corresponds to the opacity of thin icy mantle dust grains at gas densities of 10^6 cm^{-3} (Ossenkopf & Henning 1994).

In Equation (2) we assume T_{dust} equal to the NH_3 kinetic temperature, $T_{kin}^{NH_3}$, derived from NH_3 (1, 1) and (2, 2) transition lines obtained as part of the CACHMC survey (the Complete ATCA[20] Census of High-Mass Clumps; D. Allingham et al. 2022, in preparation) at $\sim5''$ angular resolution. Under typical

---

[19] This is calculated assuming an equivalent radius for a circular beam with the same area as the ALMA beam.
[20] The Australia Telescope Compact Array (ATCA; e.g., Wilson et al. 2011).

conditions prevailing in IRDCs, the gas−dust thermal coupling is effective in regions where the gas density exceeds $10^{4.5}$ cm^{-3} (e.g., Goldsmith 2001). Overall, this density threshold is fulfilled in the entire population of cores identified in ASHES (e.g., Sanhueza et al. 2019; see also the additional discussion in Section 3.3). The methodology to derive the temperature from the NH$_3$ observations is based on Mangum & Shirley (2015) and will be presented in a forthcoming paper describing the survey (D. Allingham et al. 2022, in preparation; see also Friesen et al. 2009; Hogge et al. 2018; Keown et al. 2019). The temperature maps are finally regridded to the same pixel size as the ALMA maps. We mask the native temperature maps where the error is greater than 20% of the measured $T_{\rm kin}^{\rm NH_3}$, adopting for these pixels the median $T_{\rm kin}^{\rm NH_3}$ temperature of all pixels with emission in the 1.3 mm dust continuum above 3σ (σ obtained from Sanhueza et al. 2019; see Table 1). In each source the $T_{\rm kin}^{\rm NH_3}$ ranges from ∼7 to ∼50 K, showing on average mild temperature gradients that only in some rare cases reach a few tens of kelvins within the same source. We find an average error of ∼12% $T_{\rm kin}^{\rm NH_3}$, which corresponds to ∼2 K.

The gas-to-dust ratio, γ, is computed following Giannetti et al. (2017a) with a gradient of γ through the Galactic disk:

$$\log_{10}(\gamma) = 0.087\, R_{\rm GC} + 1.44, \qquad (3)$$

where $R_{\rm GC}$ is the galactocentric distance of each source expressed in kpc (Table 1 and Whitaker et al. 2017). This prescription gives values of the gas-to-dust ratio between 69 and 87 (Table 1) and represents the second modification to the procedure followed by Sanhueza et al. (2019) to derive $N(\rm H_2)$, where γ is taken to be 100. In the worst-case scenario, this has produced a modest difference of 30% in the final $N(\rm H_2)$, but leaving unchanged their gradient across the sources. This variation agrees with the intrinsic error of 32% derived in Sanhueza et al. (2017) considering the uncertainties associated with the dust opacity and γ in the mass determination of cores and also reflects the typical error associated with $N(\rm H_2)$ considering the uncertainties on $T_{\rm dust}$ (e.g., Urquhart et al. 2018; Sanhueza et al. 2019). For this reason, we refer to Sanhueza et al. (2019) for the discussion on the distribution of $N(\rm H_2)$ in each source and for the visual inspection of the ALMA Band 6 continuum maps.

3.2. C^{18}O Column Density Maps

We derive the C^{18}O column density, $N(\rm C^{18}O)$, from its $J = 2−1$ molecular transition observed with ALMA (see Section 2.1) by following Kramer & Winnewisser (1991):

$$N(\rm C^{18}O) = \frac{3h\, C_\tau}{\eta_c\, 8\pi^3 \mu^2} f(T_{\rm ex}^{\rm C^{18}O}) \int T_b\, dv, \qquad (4)$$

with

$$f(T_{\rm ex}^{\rm C^{18}O}) = \frac{\mathcal{Z}}{2} \exp\left(\frac{E_{\rm l}}{k_{\rm B} T_{\rm ex}}\right) \left[1 - \exp\left(-\frac{h\nu_{2,1}}{k_{\rm B} T_{\rm ex}}\right)\right]^{-1}$$
$$\times\, [J(T_{\rm ex}, \nu_{2,1}) - J(T_{\rm bg}, \nu_{2,1})]^{-1}, \qquad (5)$$

where h is the Planck constant and $\eta_{\rm c}$ is the beam filling factor, assumed equal to 1. In addition, $\mu = 0.112 \times 10^{-18}$ dyn$^{0.5}$ cm^2 is the C^{18}O dipole moment, $\mathcal{Z} = 0.36\, T_{\rm ex}^{\rm C^{18}O} + 1/3$ is the partition function (e.g., Herzberg 1945), $E_{\rm l}$ is the energy

of the lower level of the transition, $T_{\rm ex}^{\rm C^{18}O}$ is the gas excitation temperature of C^{18}O, $J(T_{\rm ex}, \nu) = (h\nu/k_{\rm B})(\exp(h\nu/k_{\rm B}T_{\rm ex}) - 1)^{-1}$, $T_{\rm bg} = 2.7$ K is the background temperature, and T_b is the brightness temperature of the line. The integrated intensity is taken by considering the emission above the 3σ threshold in a range of ± 5 km s^{-1} around the $V_{\rm lsr}$ reported in Table 1.

In Equation (4), $f(T_{\rm ex}^{\rm C^{18}O})$ incorporates all the constants and the terms that depend on $T_{\rm ex}^{\rm C^{18}O}$. In addition, $C_\tau = \tau_{\rm C^{18}O}/[1 - \exp(-\tau_{\rm C^{18}O})]$ is the optical depth correction factor, valid for $\tau \leqslant 2$ with uncertainty of about 15% (e.g., Frerking et al. 1982; Kramer & Winnewisser 1991), where $\tau_{\rm C^{18}O}$ is the optical depth of the C^{18}O (2–1) line derived following the approach discussed in Sabatini et al. (2019) and summarized in Appendix A. All the molecular parameters are taken from the Cologne Database for Molecular Spectroscopy (CDMS;[21] Müller et al. 2001). In each source, the 1σ rms is computed as the average over five channels—far from the C^{18}O (2–1) line—of the flux's standard deviations computed in a large region centered at the position of the source. We solve Equation (4) under the assumption of local thermodynamic equilibrium (LTE), i.e., $T_{\rm kin}^{\rm NH_3} = T_{\rm dust} = T_{\rm ex}^{\rm C^{18}O}$. The only exception is G332.969–00.029, which lacks in available NH$_3$ data, and for which we assume $T_{\rm dust} = T_{\rm ex}^{\rm C^{18}O} = 12.6$ K as the dust temperature reported by Guzmán et al. (2015). To avoid possible overestimates of $N(\rm C^{18}O)$, produced by too low $T_{\rm ex}^{\rm C^{18}O} = T_{\rm kin}^{\rm NH_3}$ values, we impose a lower limit of $T_{\rm ex}^{\rm C^{18}O} = 10.8$ K that corresponds to the separation between the levels of the C^{18}O (2–1) transition. In the worst-case scenario, this prescription affects less than 6% of the pixels where $N(\rm C^{18}O)$ is computed. The opacity-corrected column density map of C^{18}O, also corrected for the PB effects, is shown in Appendix A. Our correction has increased $N(\rm C^{18}O)$ by up to a factor of about ∼1.8, producing $N(\rm C^{18}O)$ spanning the range of ∼(0.1–6.4) $\times 10^{16}$ cm^{-2}.

3.3. Core-scale CO-depletion Maps

The final CO-depletion factor maps, shown in Figures 1 and 2, are generated as the ratio between the expected and the observed abundance of CO relative to H$_2$, following Equation (1). For each source, we derive the expected C^{18}O/H$_2$ abundance assuming (Frerking et al. 1982; Fontani et al. 2006; Giannetti et al. 2017a)

$$X_{\rm C^{18}O}^E = \frac{9.5 \times 10^{-5} \times 10^{\alpha(R_{\rm GC} - R_{\rm GC,\odot})}}{^{16}{\rm O}/^{18}{\rm O}}, \qquad (6)$$

with $R_{\rm GC}$ expressed in kpc, $R_{\rm GC,\odot} = 8.34$ kpc (Reid et al. 2014), and $\alpha = -0.08$ dex kpc^{-1} describing the C/H abundance (Luck & Lambert 2011), under the assumption that the C/H abundance controls the CO formation.[22] The oxygen isotopic ratio, $^{16}{\rm O}/^{18}{\rm O} = 58.8 R_{\rm GC} + 37.1$, is computed according to Wilson & Rood (1994). We employ the galactocentric distances of the sources reported by Whitaker et al. (2017), according to Sanhueza et al. (2019). We find $X_{\rm C^{18}O}^E$ between 4.1×10^{-7} and 6.3×10^{-7} (see Table 1).

---

[21] https://cdms.astro.uni-koeln.de/cdms/portal/
[22] Note that the C/H abundance is given in dex units, which introduces the term 10^α in Equation (6).
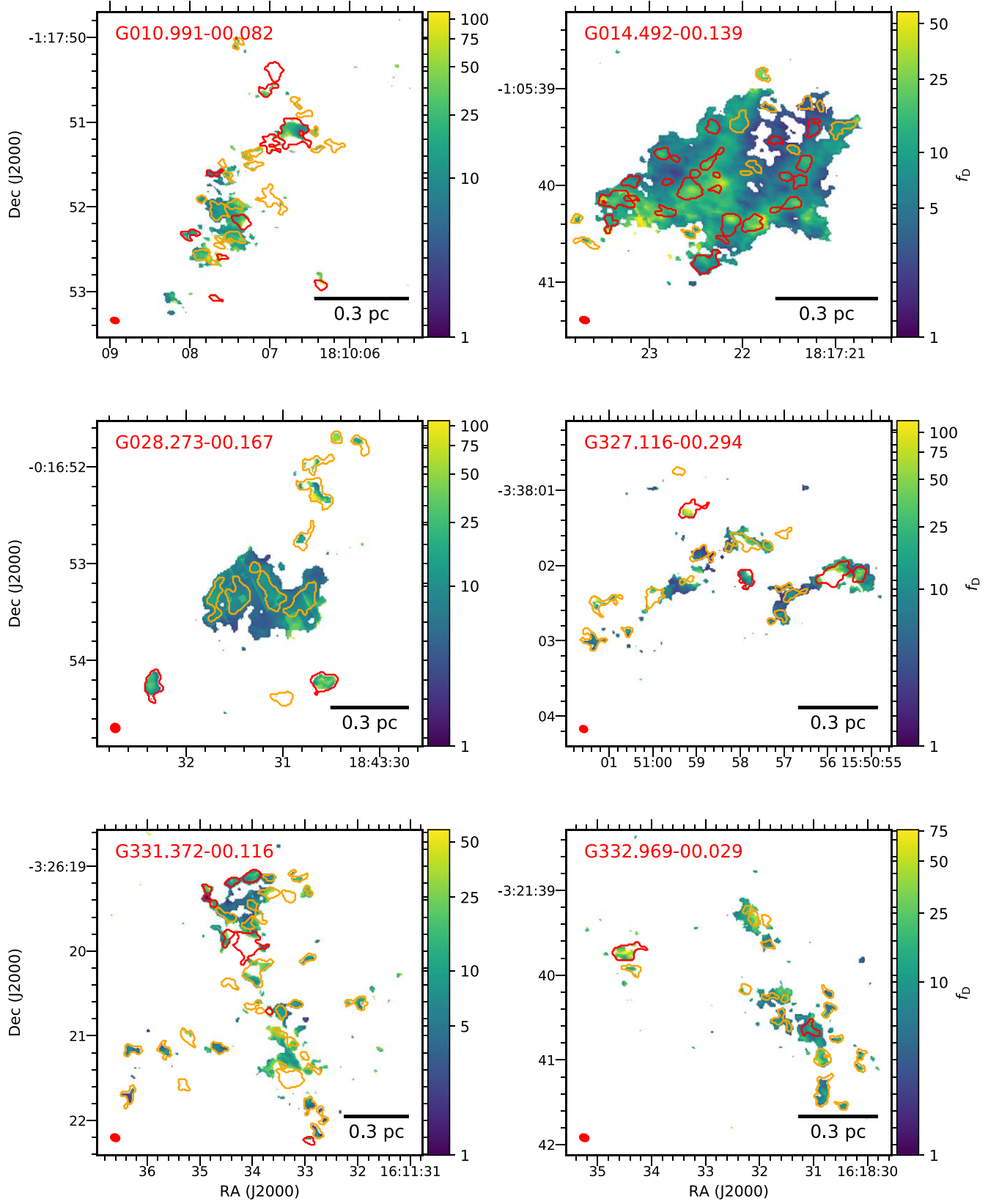
Figure 1. f_D maps obtained following the procedure explained in Section 3.3, in six of the twelve ASHES clumps (i.e. G010.991–00.082, G014.492–00.139, G028.273–00.167, G327.116-00.294, G331.372–00.116, G332.969–00.029). The cores identified in Sanhueza et al. (2019) are shown as orange and red contours for prestellar and protostar cores, respectively, following the classification in Section 2.1. The ALMA synthesized beams are displayed in red in the lower left corner of each panel, while the scale bar is shown in the lower right corners. The color wedge of each panel displays the color scales corresponding to f_D in the log-scale.
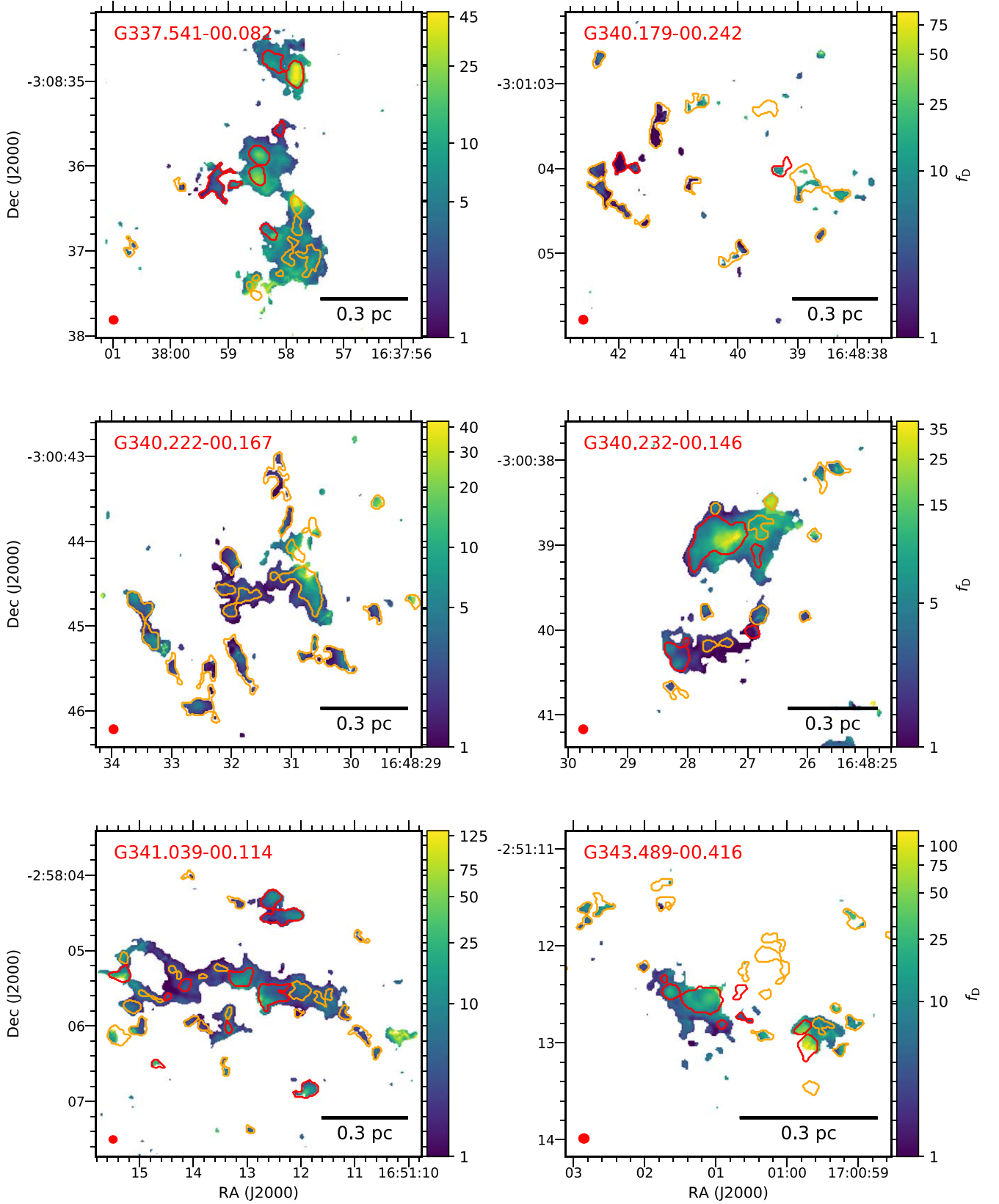
Figure 2. Same as Figure 1 for the remaining six ASHES clumps (i.e. G337.541–00.082, G340.179-00.242, G340.222-00.167, G340.232–00.146, G341.039-00.114, G343.489–00.416).

In each f_D map (Figures 1 and 2) we also report as orange/red regions the cores identified in Sanhueza et al. (2019): orange for the prestellar stage and red for the protostellar one (see Section 2).

The degree of depletion reveals widely different chemical conditions within the individual clumps. It spans regions where CO adsorption is almost irrelevant, with observed abundances of $C^{18}O$ as expected (i.e., $f_D = 1$), up to regions where only less
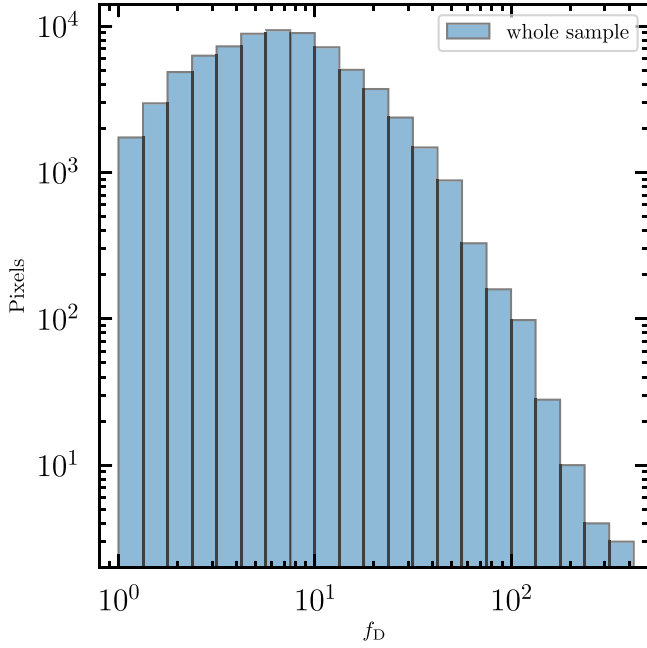
Figure 3. Number distribution of f_D mapped in Figures 1 and 2. Pixel size is 0.2″, while beam size is 1.2″.

than 1% of the expected CO is still present in the gas phase (i.e., $f_D > 100$).[23] This is clear from Figure 3, which shows the number distribution of the CO-depletion values over the entire sample. On average, in ~85% of the area mapped in f_D, more than 50% of the expected CO has been removed from the gas phase (i.e., $f_D > 2$). This is particularly relevant for the regions within the identified cores (both pre- and protostellar).

In the 12 sources shown in Figures 1 and 2, the behavior of f_D follows an unexpected increase as the evolution of the cores progresses, i.e., going from pre- to protostellar (see Table 2). As an example, G014.492−00.139 (Figure 1), with a large population of protostellar cores (i.e., 25 protostellar vs. 12 prestellar cores), shows CO depletion that is comparable to (and in some cases higher than) clumps dominated by prestellar cores (e.g., G028.273−00.167 and G340.222−00.167; Figures 1 and 2, respectively). This can be explained by exploring the physical conditions in the clumps. Due to the absence of protostars and outflows that can heat the gas surrounding the cores, these young clumps reveal mild temperature gradients. Looking at the regions associated with a $>3\sigma$ continuum emission, G028.273−00.167 and G340.222−00.167 show a $\Delta T_{\rm kin}^{\rm NH_3} \sim 1$ and ~ 3 K, respectively. If we then neglect the effect of temperature on the desorption process, it is reasonable that the evolution of the averaged f_D is mainly density driven. This is confirmed by the results reported in Figure 4(a), which show the depletion factor as a function of both density and temperature. This result also seems independent of the heliocentric distance associated with each ASHES clump, as discussed in Appendix B. From the same figure we can also see a weak temperature effect when keeping the density constant, due to the weak temperature gradients in the $T_{\rm kin}^{\rm NH_3}$ maps (see also Figure 4(b)).

---

[23] Note that some of the cores identified in dust continuum are not associated with a value of f_D (see, e.g., G010.991−00.082 and G327.116−00.294 in Figure 1). However, around those peculiar regions we find f_D among the highest over the entire clump. Thus, we expect extremely low abundances of $C^{18}O$ within those cores (therefore high f_D), below the limit of detection accessible to our observations (Table 1).
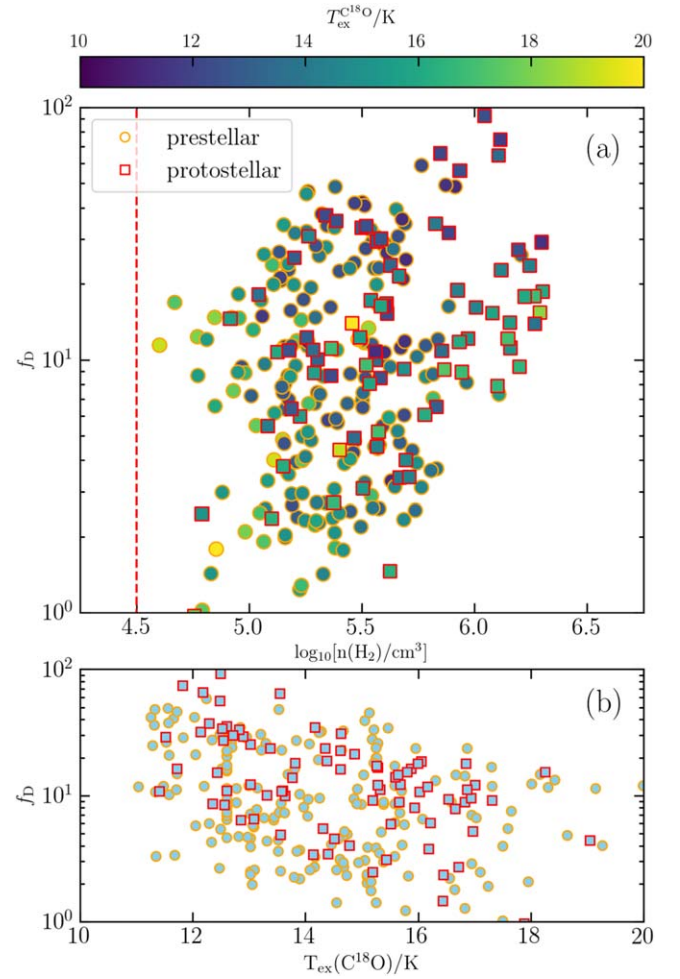

Figure 4. (a) Scatter plot of the average properties of the cores identified in ASHES. The orange circles represent the prestellar cores, while the red squares refer to the cores classified as protostellar (Section 2). The red dashed line represents the density threshold proposed by Goldsmith (2001) to ensure the gas−dust thermal coupling. (b) Average f_D vs. $T_{\rm ex}^{\rm C^{18}O}$. The gas excitation temperature of $C^{18}O$ is assumed to be equal to the kinetic temperature of NH_3.

Table 2
Averaged f_D Computed for the Whole Core Sample

Clump-ID	Core-ID[a]	$\langle f_D \rangle_{\rm core}$
G010.991−00.082	ALMA1	23.7
G010.991−00.082	ALMA2	92.8
G010.991−00.082	ALMA3	31.9
G010.991−00.082	ALMA4	...
G010.991−00.082	ALMA5	30.9
G010.991−00.082	ALMA6	56.3
G010.991−00.082	ALMA7	11.9
G010.991−00.082	ALMA8	27.6

Note.
[a] The classification of cores follows that defined in Sanhueza et al. (2019).

(This table is available in its entirety in machine-readable form.)

Within an evolutionary picture, clumps dominated by protostellar conditions are characterized by densities on average larger than the prestellar ones (e.g., König et al. 2017; Elia et al. 2021 and Urquhart et al. 2022). The same evolutionary trend is also seen at core scales (Sanhueza et al. 2019). In addition, all
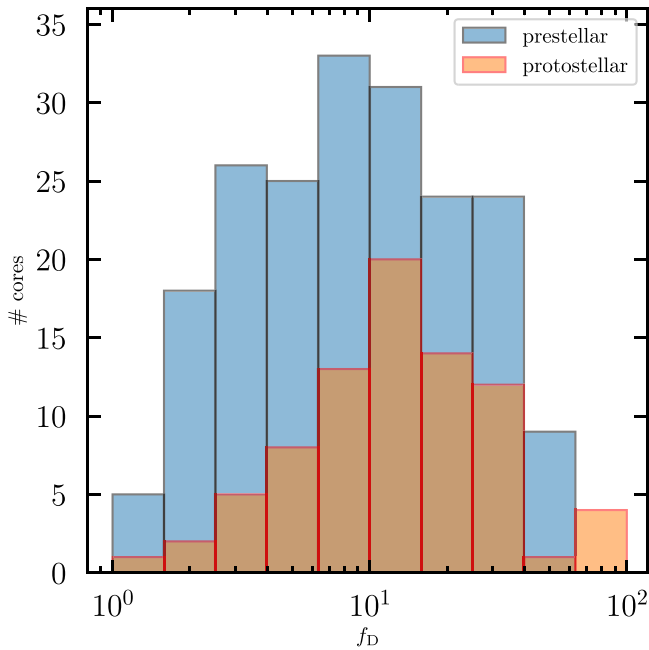
Figure 5. Number distributions of averaged f_D associated with each core identified in ASHES. The blue and orange histograms refer to prestellar and protostellar cores, respectively. A K-S two-sample test applied to the two distributions yields a p-value $< 2 \times 10^{-3}$.

the sources have been selected as $70\,\mu$m dark, and it is conceivable that the embedded protostars are at their early stages, i.e., yet to heat the surrounding gas significantly. It is then likely that the high degree of CO depletion is associated with the envelopes of these young protostellar objects, where protostellar activity has not yet led to a significant desorption of the frozen-out CO.

In Figure 5 we show the distributions of f_D for the entire population of pre- and protostellar cores in our sample (blue and orange histograms, respectively). The former show a median f_D of 8.5, while in the protostellar population we derive a median of 12.2. The protostellar distribution on average looks shifted toward higher values compared to the prestellar distribution, confirming what we observe in the maps, as well as in individual clumps (see Appendix B). This result is confirmed by a Kolmogorov–Smirnov (K-S) test (Massey 1951). The test yields a p-value $< 2 \times 10^{-3}$, which is lower than the statistical significance level of 5% usually adopted to reject the hypothesis that the two data sets come from the same continuous distribution (e.g., Teegavarapu 2019).

4. Discussion

The study of CO depletion in high-mass star-forming regions has been pursued over the years at different scales via both observations and theoretical studies. For example, the global distribution of f_D reported in Figures 1 and 2 is in agreement with the most recent state-of-the-art three-dimensional numerical simulations presented by Bovino et al. (2019), where the authors have simulated the collapse of turbulent and magnetized isothermal cores, exploring different initial conditions. They reported f_D values between 50 and 100 on a scale of 2000 au ($\sim$the effective radius associated with many of the cores identified in ASHES; Sanhueza et al. 2019), qualitatively in line with our ALMA data. Notably, the values reported by Bovino

et al. (2019) have been convolved with an ALMA-like point-spread function, showing a loss in the final f_D of a factor up to three when compared to the original simulated cubes. This might suggest the presence of compact regions where the chemistry of the CO is dramatically influenced by extreme freeze-out conditions not recoverable with our angular resolution.

On the observational side, however, a rigorous comparison with previous results is challenging, since most of the estimates of f_D, whether derived from single-point spectra (e.g., Thomas & Fuller 2008; Fontani et al. 2012; Giannetti et al. 2014) or maps (e.g., Hernandez et al. 2011; Pon et al. 2016; Feng et al. 2016a, 2020; Sabatini et al. 2019 and Gong et al. 2021), are obtained at clump-scale angular resolutions. Very few exceptions have been reported for high-mass star-forming regions (see Zhang et al. 2009; Morii et al. 2021; Rodríguez et al. 2021). Within this context our results represent the first core-scale interferometric f_D maps observed with ALMA for a sample of high-mass clumps.

In the specific case of ASHES, Morii et al. (2021) estimated f_D using additional C^{18}O (2–1) ASHES data observed in the $70\,\mu$m dark IRDC G023.477+0.114. This source is not included in this work and in the pilot study published in Sanhueza et al. (2019). G023.477+0.114 has a near-kinematic distance of 5.2 ± 0.5 kpc, which implies a linear-scale resolution of $\sim$5900 au, comparable with those of the data presented in Section 2.1. The authors consider a variation of $X^E_{C^{18}O}$ with the galactocentric distance of the source and constant values for $\gamma = 100$. They report average f_D values between $\sim$40 and 300 through the 11 cores at different evolutionary stages identified in G023.477+0.114. Notably, also in this case, f_D does not decrease going from the prestellar to the protostellar stage and shows extreme values of $f_D > 100$ associated with the most evolved sources, in agreement with our findings.

Zhang et al. (2009) conducted 1.3 mm spectral line and continuum observations of two massive molecular clumps harbored in the IRDC G28.34+0.06 (Pillai et al. 2006; Wang et al. 2008). The C^{18}O (2–1) line was observed with the Submillimeter Array (SMA; Ho et al. 2004) telescope at a resolution of $1''\!.2$ and with a final sensitivity of 90 mJy beam^{-1} at the spectral resolution of 1.2 km s^{-1}. This angular scale corresponds to $\sim$4500 au at the source heliocentric distance of 4.5 kpc (Urquhart et al. 2018), similar to the physical scales mapped in our ALMA observations. In each clump, the continuum dust emission at 1.3 mm has revealed multiple cores with typical sizes of ~ 5000 au. However, out of these cores only one shows a clear detection with an averaged value of $f_D \sim 100$ (Zhang et al. 2009). The authors assumed $\gamma = 100$ and $X^E_{C^{18}O} = 5 \times 10^{-9}$. If we rescale the f_D found for G28.34+0.06, assuming a galactocentric distance of 4.8 kpc in Equations (3) and (6),[24] we obtain an $f_D \sim 45$, which is in line with the range of values reported in Figure 3. Similarly, Rodríguez et al. (2021) observed the C^{18}O (2–1) line toward the high-mass protostellar candidate ISOSS J23053+5953 SMM2 with SMA at $\sim 2''\!.5$ ($\sim 10^4$ au at the distance of 4.3 kpc). They report $f_D \sim 20$, already considering the variation of γ and $X^E_{C^{18}O}$ with galactocentric distance of the source (~ 10 kpc Bosco et al. 2019).

It is worth noting that both the sources of Zhang et al. (2009) and Rodríguez et al. (2021) host mYSOs as demonstrated by

---

[24] Taking a brightness temperature of 2.5 K, an FWHM of 2.5 km s^{-1}, a gas temperature of 30 K as reported by Zhang et al. (2009) for the detected C^{18}O (2–1) line, and the derived $\gamma = 72$ and $X^E_{C^{18}O} = 5.7 \times 10^{-7}$.
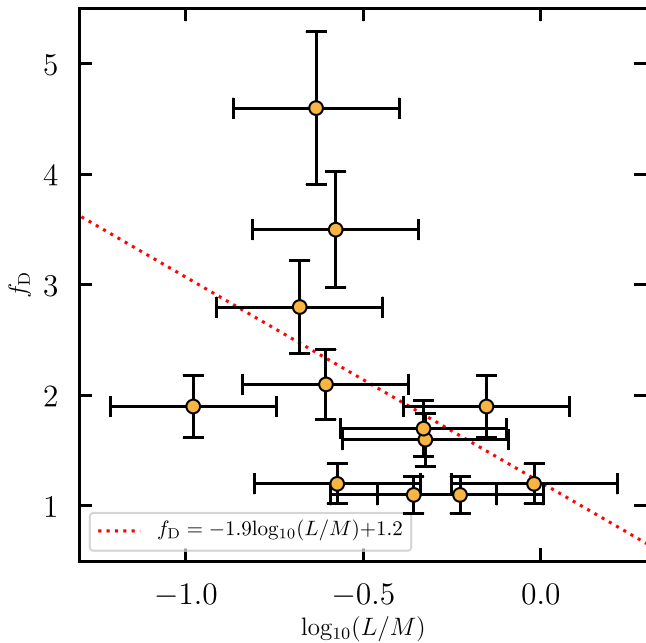
Figure 6. Correlation between f_D and the luminosity-to-mass ratio of the clumps that compose the ASHES sample. Yellow circles are associated with each source, while uncertainties are shown as black bars. The red dashed line represents the linear least-squares fit of f_D to the $\log_{10}(L/M)$. The fit parameters are shown in the legend, with Spearman's rank correlation coefficient $\rho_s = -0.62$ and a p-value $= 0.03$.

the 24 μm emission peaks and/or the presence of hot molecular cores with already-developed outflows/jets. These high values observed in advanced evolutionary stages provide further evidence that on core scales the degree of CO depletion may not be suitable to follow the evolution of a core owing to the huge amount of cold molecular gas that can surround an mYSO. These high densities could also increase the efficiency of dust grain coagulation (Galametz et al. 2019), implying a larger grain size and, in turn, decreasing the heating and subsequent evaporation of CO from the surface of the dust grains (Iqbal & Wakelam 2018).

Across the whole clump scale, however, the revealed chemical picture changes. We have calculated the average f_D of each clump shown in Figure 1 and 2, after convolving the $N(\mathrm{H}_2)$ and $N(\mathrm{C}^{18}\mathrm{O})$ maps to an angular resolution equal to the effective radius of each clump (see Table 1). We associate with this derivation a conservative error of 15% that accounts for the fluctuations observed for f_D over the wide range of densities and temperatures found on the molecular cloud scale (Sabatini et al. 2019). We have correlated the average f_D of each source with the corresponding luminosity-to-mass ratio (L/M) of the clumps, a well-known distance-independent evolutionary indicator for both low- and high-mass star-forming regions (e.g., Saraceno et al. 1996; Molinari et al. 2008; Urquhart et al. 2022). The bolometric luminosity, L, and clump mass, M, are taken from Li et al. (2020) with associated errors of 50% for L and 20% for M, respectively (Urquhart et al. 2018). These uncertainties have been derived from a statistical relevant sample of $\sim 10^4$ high-mass clumps identified in the APEX Telescope Large Area Survey of the Galaxy (Schuller et al. 2009).

Figure 6 shows the results of this correlation, presenting a clear downward trend of f_D with increasing L/M. A linear least-squares fit of f_D to the $\log_{10}(L/M)$ is shown as a red dashed line in the same figure. The averaged f_D is found to change by a

factor of ~ 5 for about one order of magnitude in L/M, yielding the power-law relation $f_D = -1.9 \log_{10}(L/M) + 1.2$, with a Spearman's rank correlation coefficient $\rho_s = -0.62$ and a p-value $= 0.03$ (e.g., Zwillinger & Kokoska 2000; Cohen 1988). This result confirms the reliability of f_D to classify high-mass clumps at different evolutionary stages, as found in several samples (e.g., Fontani et al. 2012; Giannetti et al. 2014; Sabatini et al. 2019). The different behavior of f_D observed at clump and core scale might be the consequence of the complex interplay between chemistry and physics and their associated timescales. In particular, the chemical response to physical changes is smeared out when looking at clump scales, reflecting the average properties of the entire population of cores.

5. Conclusions

In this paper we presented the first core-scale f_D maps derived from $\mathrm{C}^{18}\mathrm{O}$ (2–1) and 1.3 mm continuum ALMA observations for the 12 70 μm dark clumps of the ASHES sample. In this context, we have discussed whether the averaged CO-depletion factor computed at core scales can be considered a reliable evolutionary indicator of the high-mass star formation process.

The overall scenario that emerged from this study shows peculiar chemical conditions for the ISM involved in our targets, which changes according to the physical scale investigated. On the clump scale, we find that on average at least half of the expected CO has been removed from the gas phase, for more than 85% of the total area mapped in $\mathrm{C}^{18}\mathrm{O}$. The highest values of CO depletion are found within the identified cores (both pre- and protostellar), where f_D values of more than 10 are reached in more than $\sim 50\%$ of the cores.

In contrast to what has been observed for low-mass star-forming cores and, more generally, for high-mass clumps that have the potential to form high-mass stars, our analysis shows that the degree of the CO-depletion process on core scales does not decrease during the transition from a prestellar to a protostellar phase. If we exclude the temperature effect due to the slight gradients in the $T_{\mathrm{kin}}^{\mathrm{NH}_3}$ maps, we explain the evolutionary behavior of f_D as primarily dependent on the average gas density, which increases with the evolution of the cores. This effect is not observed in the low-mass regime since the high-density regions have smaller sizes and are more affected by temperature variations driven by the star formation process. Furthermore, low-mass star-forming regions are also statistically closer to the solar system, allowing for a better linear resolution. We emphasize that, due to the poorer resolution of the NH$_3$ maps (on average a factor ~ 4 coarser) compared to those of $\mathrm{C}^{18}\mathrm{O}$, temperature is also one of the main uncertainties affecting our results. Our analysis could greatly benefit from ammonia observations with a resolution comparable to that of ALMA. Nevertheless, we highlight the significant improvement for having derived temperatures at $\sim 5''$ angular resolution with respect to adopting the Herschel dust temperatures at $35''$ resolution.

The f_D fluctuations appear to be widely distributed when observed over thousands of astronomical units, and in particular they trace the densest regions of clumps that are not always associated with a prestellar core. Our results lead us to classify f_D as a tracer that is not entirely reliable to distinguishing between prestellar and protostellar cores in high-mass star-forming clumps. However, thanks to the high CO-depletion factors found in large parts of the clump, a more

complete picture of evolution can be obtained by observing deuterated molecules. The abundance of ortho-H_2D^+, for example, has been asserted as a clear chemical indicator of prestellar stages both at the clump scale (e.g., Giannetti et al. 2019; Miettinen 2020 and Sabatini et al. 2020) and at the core scales by the recent results of Redaelli et al. (2021) and Redaelli et al. (2022) obtained from ALMA data. Improving the sensitivity of astronomical facilities in the millimeter and submillimeter regime (such as APEX and ALMA) and the systematic study of deuterated molecules (such as H_2D^+ and D_2H^+) therefore seems to be the necessary breakthrough to finally obtain a comprehensive picture of the process of high-mass star formation.

Appendix A
$C^{18}O$ Opacity Correction

When deriving the $N(C^{18}O)$, it is worth inspecting whether the emission of $C^{18}O$ (2–1) can be assumed to be optically thin.

The optical depth of a transition can be estimated through the peak ratio of the same transition, coming from different isotopologues, if their relative abundance is known (e.g., Hofner et al. 2000). We computed $\tau_{C^{18}O}$ using $C^{17}O$ (2–1), $C^{18}O$ (2–1), and H_2 data published in Feng et al. (2020) observed in G014.492–00.139, and we refer to this paper for a more detailed description of the data set. We selected this source since the final $N(H_2)$ are among the highest of the entire ASHES sample, and therefore G014.492–00.139 represents an ideal case to study the variation of $\tau_{C^{18}O}$.

Assuming equal excitation temperatures and filling factor for the two species, $\tau_{C^{18}O}$ is estimated as

$$R_{18,17} = \frac{T_{mb}^{C^{18}O}}{T_{mb}^{C^{17}O}} \propto \frac{[1 - \exp(-\tau_{C^{18}O})]}{[1 - \exp(-\tau_{C^{17}O})]}, \qquad (A1)$$

where $\tau_{C^{17}O}$ is the optical depth of $C^{17}O$ (2–1) at $\sim$224.7 GHz, for which we assume $\tau_{C^{17}O} = \tau_{C^{18}O}/4.16$ (e.g., Wouterloot et al. 2008). The fit is performed pixel by pixel for both $C^{17}O$ and $C^{18}O$ data cubes by taking data where both the continuum and the line emission have a $>3\sigma$ level detection. We employ the Python Spectroscopic Toolkit (PySpecKit; Ginsburg & Mirocha 2011; Ginsburg et al. 2022), by using a single Gaussian component over a velocity space of ±3 km s^{-1} around the local standard of rest velocities (V_{lsr}) derived in Sanhueza et al. (2019). The estimated $\tau_{C^{18}O}$ are in the range of $\sim$0.25–1.80, implying optical depth correction factors $C_\tau \in \{1.13$–$2.16\}$ to derive the final $N(C^{18}O)$ from Equation (4). In more than 75% of the sources detected in $C^{18}O$, $\tau_{C^{18}O} < 1.37$ ($C_\tau < 1.84$). Similar $\tau_{C^{18}O}$ are also reported in other IRDCs (e.g., Sanhueza et al. 2010; Sabatini et al. 2019; Gong et al. 2021), proving that $C^{18}O$ is virtually always optically thin under the typical conditions prevalent in IRDCs.

To account for the same correction in the other ASHES sources, we follow the same approach as Sabatini et al. (2019), looking for a linear relation between $\log_{10}(\tau_{C^{18}O})$ and $\log_{10}[N(H_2)]$. We have preferred the H_2 column density over $N(C^{18}O)$ since $N(H_2)$ is not affected by opacity at the observed size scales (i.e., κ_ν correction already applied in Section 3.1). The final $C^{18}O$ column density maps (see Figures 7 and 8) are derived applying in each source the best-fit $\log_{10}(\tau_{C^{18}O})$-$\log_{10}[N(H_2)]$ relation obtained in G014.492–00.139, i.e., $\log_{10}(\tau_{C^{18}O}) = 0.6\log_{10}[N(H_2)] - 14.4$.
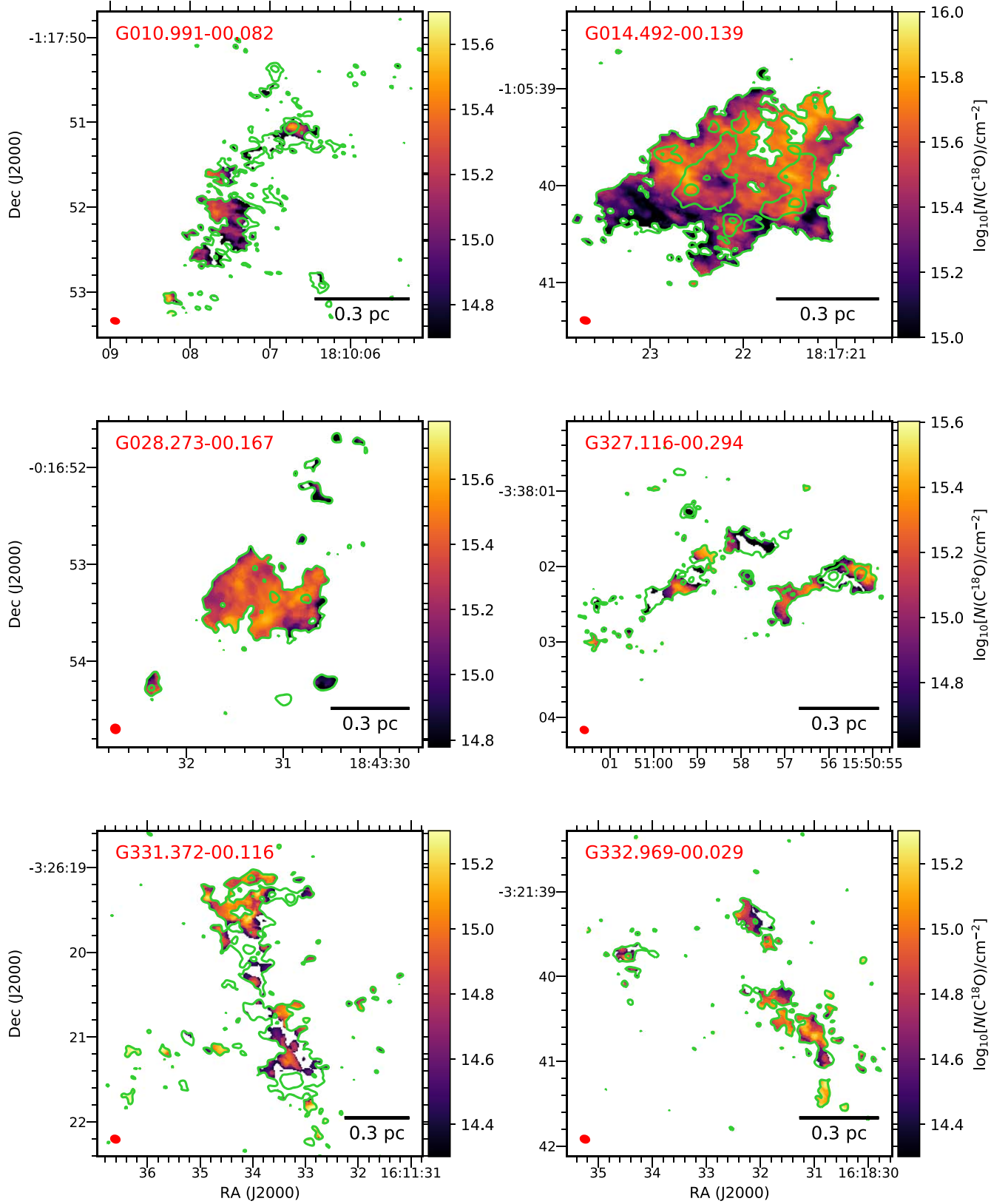
Figure 7. Final $N(C^{18}O)$ maps obtained following the procedure explained in Section 3.2, in six of the twelve ASHES clumps (i.e. G010.991–00.082, G014.492–00.139, 'G028.273–00.167, G327.116-00.294, G331.372–00.116, G332.969–00.029). All the maps are corrected for opacity effects as reported in Appendix A. Green contours correspond to the ALMA dust continuum emission at $[3,9,27] \times \sigma$ (Sanhueza et al. 2019). The ALMA synthesized beams are displayed in red in the lower left corner of each panel, while the scale bar is shown in the lower right corners. The color wedge of each panel displays the color scales corresponding to $N(C^{18}O)$ in the log-scale.
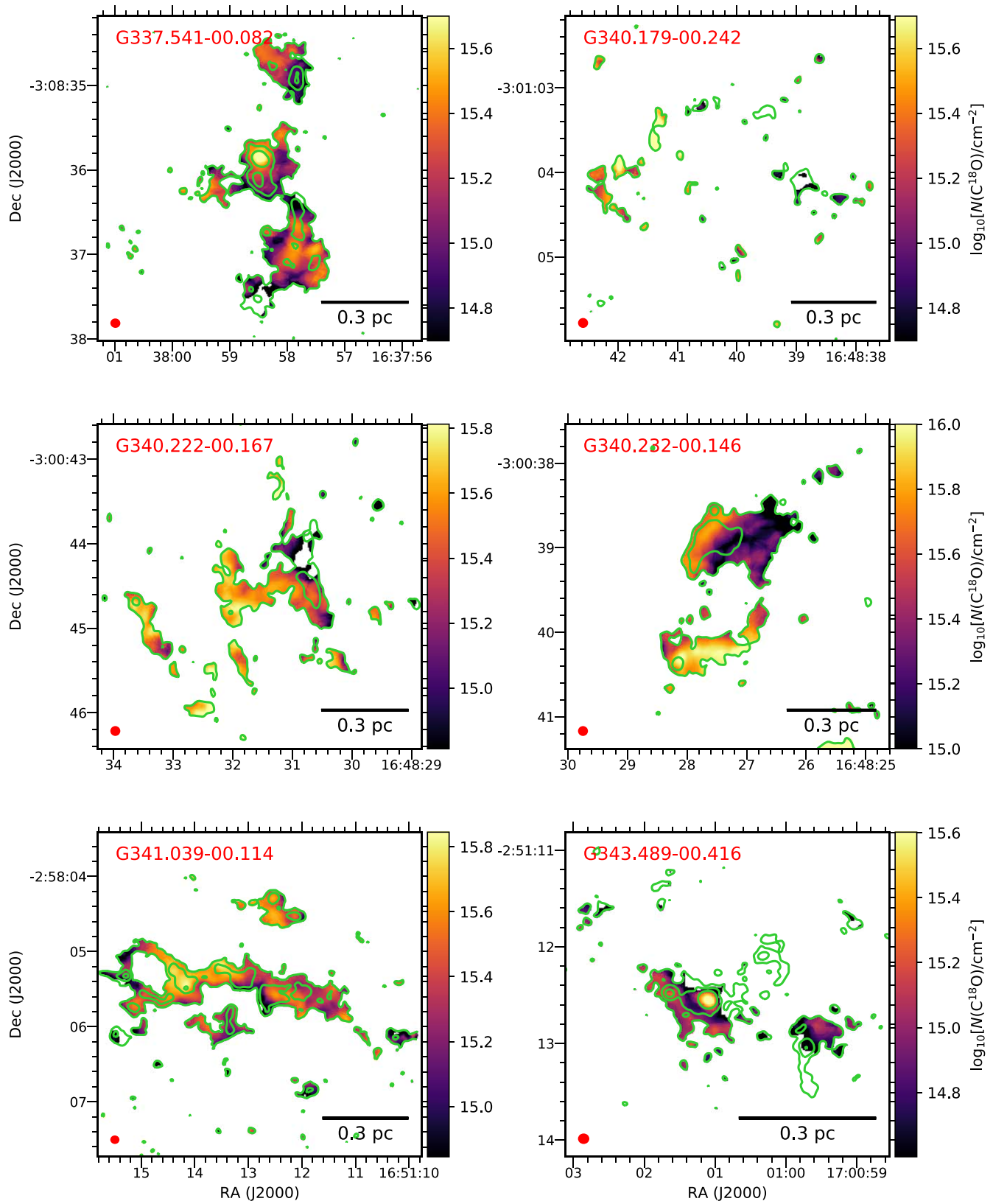
Figure 8. Same as Figure 7 for the remaining six ASHES clumps (i.e. G337.541–00.082, G340.179-00.242, G340.222-00.167, G340.232–00.146, G341.039-00.114, G343.489–00.416).

Appendix B
Notes on the Analysis for Individual Clumps

The aim of this section is to test the influence of some specific properties of the clumps on the results discussed in Sections 3.3 and 4 (e.g., the heliocentric distance of the clumps, the number of cores, or the proportion of pre- and protostellar cores found in each ASHES source).

Figure 9 represents the analog of Figure 4, in which we have colored the cores as a function of the heliocentric distance of the clumps hosting them. There is no clustering of cores when the distance of each source is considered, and the cores associated with each distance bin span comparable ranges of values in terms of f_D and $n(H_2)$, corresponding to at least a factor of $\sim$5. Thus, the distribution of cores shown in Figure 4

appears to be distance independent, ruling out the influence of a possible distance bias on our results.

Figure 10 represents the analog of Figure 5 and shows the number distributions of the averaged f_D associated with ASHES cores within each clump separately. Although the statistics of the cores in each clump is greatly reduced compared to the total number of cores shown in Figure 5, we note that the median value of f_D derived for the prestellar population of cores (blue vertical lines in Figure 10) is always lower than—or at most equal to—the value found for the protostellar cores (red dashed vertical lines; Figure 10). Figure 10 also shows that randomly removing a clump from the analysis presented in Sections 3.3 and 4 does not qualitatively change the general conclusions summarized in Section 5.
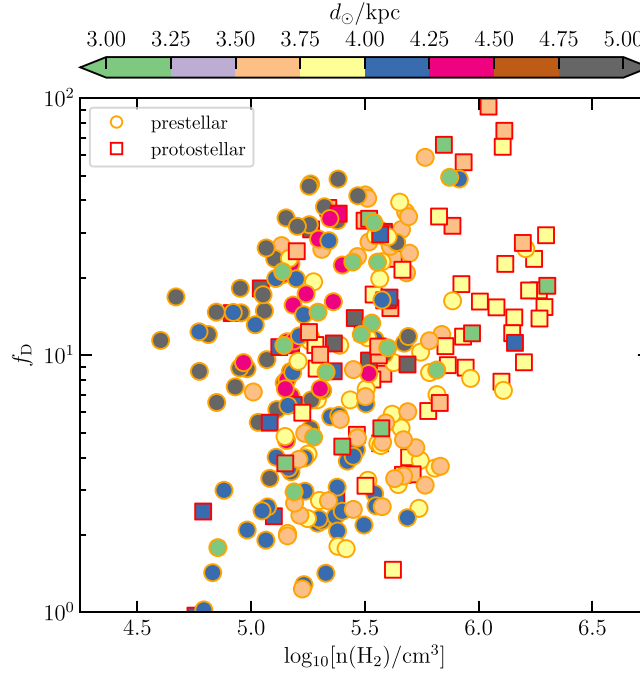
Figure 9. Same as Figure 4(a), but showing the variation in the average f_D and $n(H_2)$ for the core population identified in ASHES as a function of the heliocentric distance of each clump (indicated in the color wedge; see also Table 1). Circles and squares represent the prestellar and protostellar cores, respectively.
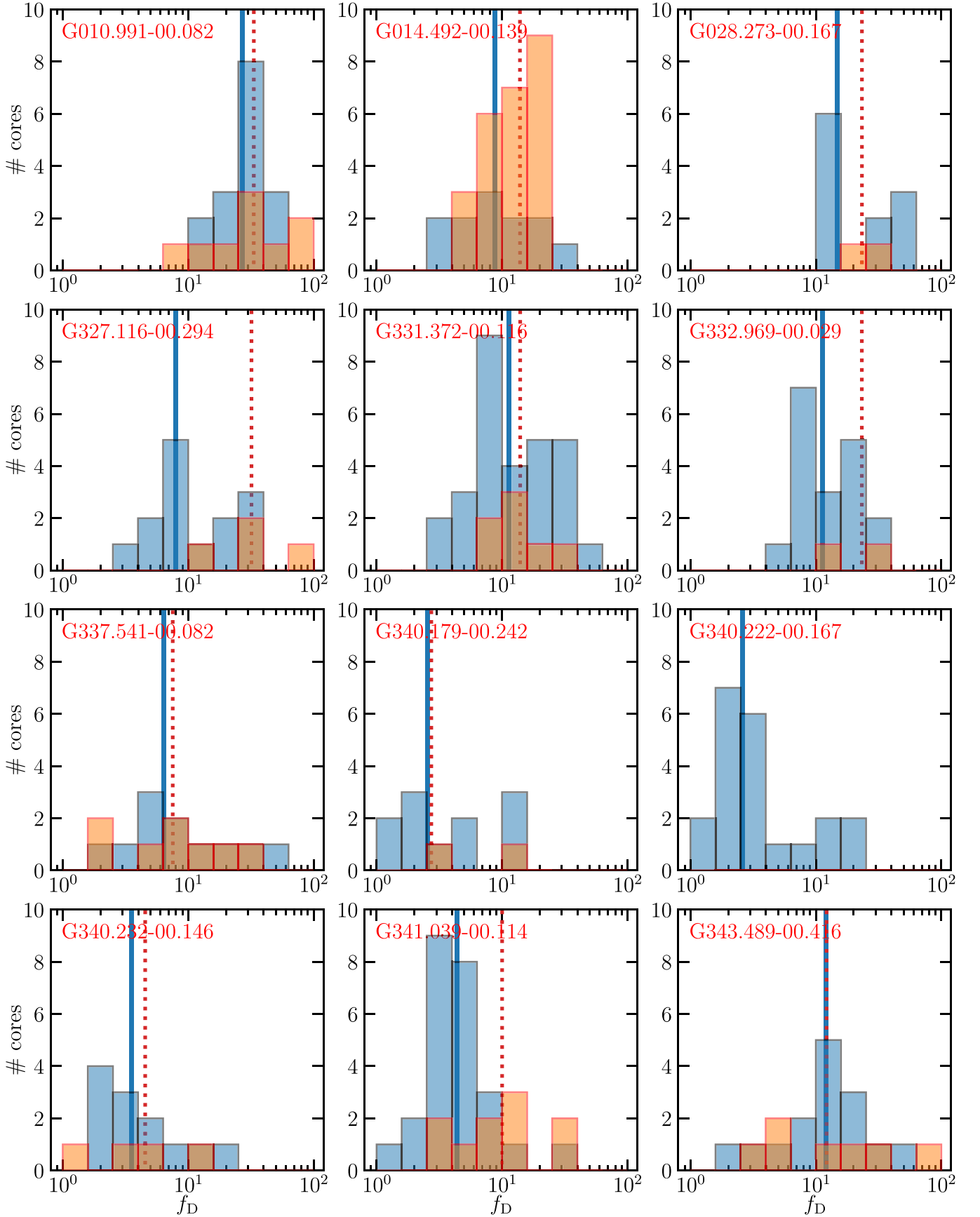
Figure 10. Same as Figure 5, but showing the number distributions of the averaged f_D associated with each core identified in ASHES. In the different panels, the distributions within each clump are shown separately (red labels in the upper left corners). The blue and orange histograms refer to prestellar and protostellar cores, respectively. The vertical lines represent the median of f_D resulting from the distributions of prestellar (blue lines) and protostellar (red dashed lines) cores.

ORCID iDs

Giovanni Sabatini ● https://orcid.org/0000-0002-6428-9806
Stefano Bovino ● https://orcid.org/0000-0003-2814-6688
Patricio Sanhueza ● https://orcid.org/0000-0002-7125-7685
Kaho Morii ● https://orcid.org/0000-0002-6752-6061
Shanghuo Li ● https://orcid.org/0000-0003-1275-5251
Elena Redaelli ● https://orcid.org/0000-0002-0528-8125
Qizhou Zhang ● https://orcid.org/0000-0003-2384-6589
Xing Lu ● https://orcid.org/0000-0003-2619-9305
Siyi Feng ● https://orcid.org/0000-0002-4707-8409
Daniel Tafoya ● https://orcid.org/0000-0002-2149-2660
Natsuko Izumi ● https://orcid.org/0000-0003-1604-9127
Takeshi Sakai ● https://orcid.org/0000-0003-4521-7492
Ken'ichi Tatematsu ● https://orcid.org/0000-0002-8149-8546
David Allingham ● https://orcid.org/0000-0002-4173-2852

References

Adams, F. C. 2010, ARA&A, 48, 47
Astropy Collaboration, Price-Whelan, A. M., Sipőcz, B. M., et al. 2018, AJ, 156, 123
Astropy Collaboration, Robitaille, T. P., Tollerud, E. J., et al. 2013, A&A, 558, A33
Battersby, C., Bally, J., Jackson, J. M., et al. 2010, ApJ, 721, 222
Bergin, E. A., Alves, J., Huard, T., & Lada, C. J. 2002, ApJL, 570, L101
Bonnell, I. A., Bate, M. R., Clarke, C. J., & Pringle, J. E. 2001, MNRAS, 323, 785
Bosco, F., Beuther, H., Ahmadi, A., et al. 2019, A&A, 629, A10
Bovino, S., Ferrada-Chamorro, S., Lupi, A., et al. 2019, ApJ, 887, 224
Carey, S. J., Clark, F. O., Egan, M. P., et al. 1998, ApJ, 508, 721
Carey, S. J., Noriega-Crespo, A., Mizuno, D. R., et al. 2009, PASP, 121, 76
Caselli, P., Vastel, C., Ceccarelli, C., et al. 2008, A&A, 492, 703
Caselli, P., Walmsley, C. M., Tafalla, M., Dore, L., & Myers, P. C. 1999, ApJL, 523, L165
Cesaroni, R. 2005, in IAU Symp. 227, Massive Star Birth: A Crossroads of Astrophysics, ed. R. Cesaroni (Cambridge: Cambridge Univ. Press), 59
Chambers, E. T., Jackson, J. M., Rathborne, J. M., & Simon, R. 2009, ApJS, 181, 360
Chevance, M., Krumholz, M. R., McLeod, A. F., et al. 2022, arXiv:2203.09570
Cohen, J. 1988, Statistical Power Analysis for the Behavioral Sciences (New York: Routledge)
Contreras, Y., Rathborne, J. M., Guzman, A., et al. 2017, MNRAS, 466, 340
Contreras, Y., Sanhueza, P., Jackson, J. M., et al. 2018, ApJ, 861, 14
Egan, M. P., Shipman, R. F., Price, S. D., et al. 1998, ApJL, 494, L199
Elia, D., Merello, M., Molinari, S., et al. 2021, MNRAS, 504, 2742
Elia, D., Molinari, S., Schisano, E., et al. 2017, MNRAS, 471, 100
Elmegreen, B. G. 1998, in ASP Conf. Ser. 148, Origins, ed. C. E. Woodward et al. (San Francisco, CA: ASP), 150
Feng, S., Beuther, H., Zhang, Q., et al. 2016a, A&A, 592, A21
Feng, S., Beuther, H., Zhang, Q., et al. 2016b, ApJ, 828, 100
Feng, S., Li, D., Caselli, P., et al. 2020, ApJ, 901, 145
Fontani, F., Caselli, P., Crapsi, A., et al. 2006, A&A, 460, 709
Fontani, F., Giannetti, A., Beltrán, M. T., et al. 2012, MNRAS, 423, 2342
Frerking, M. A., Langer, W. D., & Wilson, R. W. 1982, ApJ, 262, 590
Friesen, R. K., Di Francesco, J., Shirley, Y. L., & Myers, P. C. 2009, ApJ, 697, 1457
Galametz, M., Maury, A. J., Valdivia, V., et al. 2019, A&A, 632, A5
Giannetti, A., Bovino, S., Caselli, P., et al. 2019, A&A, 621, L7
Giannetti, A., Leurini, S., König, C., et al. 2017a, A&A, 606, L12
Giannetti, A., Leurini, S., Wyrowski, F., et al. 2017b, A&A, 603, A33
Giannetti, A., Wyrowski, F., Brand, J., et al. 2014, A&A, 570, A65
Ginsburg, A., Darling, J., Battersby, C., Zeiger, B., & Bally, J. 2022, AJ, 163, 291
Ginsburg, A., & Mirocha, J. 2011, PySpecKit: Python Spectroscopic Toolkit, Astrophysics Source Code Library, ascl:1109.001
Goldsmith, P. F. 2001, ApJ, 557, 736
Gong, Y., Belloche, A., Du, F. J., et al. 2021, A&A, 646, A170
Güsten, R., Nyman, L. Å., Schilke, P., et al. 2006, A&A, 454, L13
Guzmán, A. E., Sanhueza, P., Contreras, Y., et al. 2015, ApJ, 815, 130
Harris, C. R., Millman, K. J., van der Walt, S. J., et al. 2020, Natur, 585, 357
Herbst, E., & van Dishoeck, E. F. 2009, ARA&A, 47, 427

Hernandez, A. K., Tan, J. C., Caselli, P., et al. 2011, ApJ, 738, 11
Herzberg, G. 1945, Molecular Spectra and Molecular Structure. Vol.2: Infrared and Raman Spectra of Polyatomic Molecules (New York: Wiley)
Heyer, M., & Dame, T. M. 2015, ARA&A, 53, 583
Ho, P. T. P., Moran, J. M., & Lo, K. Y. 2004, ApJ, 616, L1
Hoare, M. G., Purcell, C. R., Churchwell, E. B., et al. 2012, PASP, 124, 939
Hofner, P., Wyrowski, F., Walmsley, C. M., & Churchwell, E. 2000, ApJ, 536, 393
Hogge, T., Jackson, J., Stephens, I., et al. 2018, ApJS, 237, 27
Hunter, J. D. 2007, CSE, 9, 90
Iguchi, S., Morita, K.-I., Sugimoto, M., et al. 2009, PASJ, 61, 1
Iqbal, W., & Wakelam, V. 2018, A&A, 615, A20
Kauffmann, J., Bertoldi, F., Bourke, T. L., Evans, N. J. I., & Lee, C. W. 2008, A&A, 487, 993
Keown, J., Di Francesco, J., Rosolowsky, E., et al. 2019, ApJ, 884, 4
König, C., Urquhart, J. S., Csengeri, T., et al. 2017, A&A, 599, A139
Kramer, C., Alves, J., Lada, C. J., et al. 1999, A&A, 342, 257
Kramer, C., & Winnewisser, G. 1991, A&AS, 89, 421
Kumar, M. S. N., Palmeirim, P., Arzoumanian, D., & Inutsuka, S. I. 2020, A&A, 642, A87
Kurtz, S., Cesaroni, R., Churchwell, E., Hofner, P., & Walmsley, C. M. 2000, in Protostars and Planets IV, ed. V. Mannings, A. P. Boss, & S. S. Russell (Tucson, AZ: Univ. Arizona Press), 299
Li, S., Sanhueza, P., Lee, C. W., et al. 2022, ApJ, 926, 165
Li, S., Sanhueza, P., Zhang, Q., et al. 2020, ApJ, 903, 119
Li, S., Zhang, Q., Pillai, T., et al. 2019, ApJ, 886, 130
Luck, R. E., & Lambert, D. L. 2011, AJ, 142, 136
Mangum, J. G., & Shirley, Y. L. 2015, PASP, 127, 266
Massey, F. J. 1951, J Am. Stat. Assoc., 46, 68
McKee, C. F., & Tan, J. C. 2002, Natur, 416, 59
Miettinen, O. 2020, A&A, 634, A115
Molinari, S., Pezzuto, S., Cesaroni, R., et al. 2008, A&A, 481, 345
Molinari, S., Swinyard, B., Bally, J., et al. 2010, PASP, 122, 314
Morii, K., Sanhueza, P., Nakamura, F., et al. 2021, ApJ, 923, 147
Müller, H. S. P., Thorwirth, S., Roth, D. A., & Winnewisser, G. 2001, A&A, 370, L49
Ossenkopf, V., & Henning, T. 1994, A&A, 291, 943
Padoan, P., Pan, L., Juvela, M., Haugbølle, T., & Nordlund, Å. 2020, ApJ, 900, 82
Perault, M., Omont, A., Simon, G., et al. 1996, A&A, 315, L165
Peretto, N., Lenfestey, C., Fuller, G. A., et al. 2016, A&A, 590, A72
Pilbratt, G. L., Riedinger, J. R., Passvogel, T., et al. 2010, A&A, 518, L1
Pillai, T., Wyrowski, F., Carey, S. J., & Menten, K. M. 2006, A&A, 450, 569
Pillai, T., Wyrowski, F., Hatchell, J., Gibb, A. G., & Thompson, M. A. 2007, A&A, 467, 207
Pokhrel, R., Myers, P. C., Dunham, M. M., et al. 2018, ApJ, 853, 5
Pon, A., Johnstone, D., Caselli, P., et al. 2016, A&A, 587, A96
Price, S. D., Egan, M. P., Carey, S. J., Mizuno, D. R., & Kuchar, T. A. 2001, AJ, 121, 2819
Rathborne, J. M., Jackson, J. M., & Simon, R. 2006, ApJ, 641, 389
Redaelli, E., Bovino, S., Giannetti, A., et al. 2021, A&A, 650, A202
Redaelli, E., Bovino, S., Sanhueza, P., et al. 2022, ApJ, in press, arXiv:2208.01675
Reid, M. J., Menten, K. M., Brunthaler, A., et al. 2014, ApJ, 783, 130
Rieke, G. H., Young, E. T., Engelbracht, C. W., et al. 2004, ApJS, 154, 25
Robitaille, T., & Bressert, E. 2012, APLpy: Astronomical Plotting Library in Python, Astrophysics Source Code Library, ascl:1208.017
Rodríguez, T. M., Hofner, P., Araya, E. D., et al. 2021, ApJ, 922, 66
Sabatini, G., Bovino, S., Giannetti, A., et al. 2020, A&A, 644, A34
Sabatini, G., Bovino, S., Giannetti, A., et al. 2021, A&A, 652, A71
Sabatini, G., Giannetti, A., Bovino, S., et al. 2019, MNRAS, 490, 4489
Sakai, T., Sanhueza, P., Furuya, K., et al. 2022, ApJ, 925, 144
Sanhueza, P., Contreras, Y., Wu, B., et al. 2019, ApJ, 886, 102
Sanhueza, P., Garay, G., Bronfman, L., et al. 2010, ApJ, 715, 18
Sanhueza, P., Jackson, J. M., Foster, J. B., et al. 2012, ApJ, 756, 60
Sanhueza, P., Jackson, J. M., Foster, J. B., et al. 2013, ApJ, 773, 123
Sanhueza, P., Jackson, J. M., Zhang, Q., et al. 2017, ApJ, 841, 97
Saraceno, P., Andre, P., Ceccarelli, C., Griffin, M., & Molinari, S. 1996, A&A, 309, 827
Schuller, F., Menten, K. M., Contreras, Y., et al. 2009, A&A, 504, 415
Simon, R., Jackson, J. M., Rathborne, J. M., & Chambers, E. T. 2006a, ApJ, 639, 227
Simon, R., Rathborne, J. M., Shah, R. Y., Jackson, J. M., & Chambers, E. T. 2006b, ApJ, 653, 1325
Tafoya, D., Sanhueza, P., Zhang, Q., et al. 2021, ApJ, 913, 131

Teegavarapu, R. S. 2019, in Trends and Changes in Hydroclimatic Variables, ed. R. Teegavarapu (Amsterdam: Elsevier), 1, https://www.elsevier.com/books/trends-and-changes-in-hydroclimatic-variables/teegavarapu/978-0-12-810985-4

Thomas, H. S., & Fuller, G. A. 2008, A&A, 479, 751

Tigé, J., Motte, F., Russeil, D., et al. 2017, A&A, 602, A77

Urquhart, J. S., Hoare, M. G., Purcell, C. R., et al. 2009, A&A, 501, 539

Urquhart, J. S., König, C., Giannetti, A., et al. 2018, MNRAS, 473, 1059

Urquhart, J. S., Wells, M. R. A., Pillai, T., et al. 2022, MNRAS, 510, 3389

Wang, K., Zhang, Q., Testi, L., et al. 2014, MNRAS, 439, 3275

Wang, Y., Zhang, Q., Pillai, T., Wyrowski, F., & Wu, Y. 2008, ApJL, 672, L33

Whitaker, J. S., Jackson, J. M., Rathborne, J. M., et al. 2017, AJ, 154, 140

Wiles, B., Lo, N., Redman, M. P., et al. 2016, MNRAS, 458, 3429

Wilson, T. L., & Rood, R. 1994, ARA&A, 32, 191

Wilson, W. E., Ferris, R. H., Axtens, P., et al. 2011, MNRAS, 416, 832

Wootten, A., & Thompson, A. R. 2009, IEEE Proc., 97, 1463

Wouterloot, J. G. A., Henkel, C., Brand, J., & Davis, G. R. 2008, A&A, 487, 237

Zhang, Q., & Wang, K. 2011, ApJ, 733, 26

Zhang, Q., Wang, Y., Pillai, T., & Rathborne, J. 2009, ApJ, 696, 268

Zhang, Y., Tan, J. C., & Hosokawa, T. 2014, ApJ, 788, 166

Zwillinger, D., & Kokoska, S. 2000, CRC Standard Probability and Statistics Tables and Formulae (Boca Raton, FL: CRC Press), http://tomlr.free.fr/Math%E9matiques/Math%20Complete/Probability%20and%20statistics/CRC%20-%20standard%20probability%20and%20Statistics%20tables%20and%20formulae%20-%20DANIEL%20ZWILLINGER.pdf